



# Strong electronic coupling between ruthenium single atoms and ultrafine nanoclusters enables economical and effective hydrogen production

Hanxu Yao<sup>a,b,1</sup>, Xingkun Wang<sup>a,1</sup>, Kai Li<sup>c,1</sup>, Cheng Li<sup>d,e,1</sup>, Canhui Zhang<sup>a</sup>, Jian Zhou<sup>b</sup>, Zhengwen Cao<sup>b</sup>, Huanlei Wang<sup>a</sup>, Meng Gu<sup>d</sup>, Minghua Huang<sup>a,\*</sup>, Heqing Jiang<sup>b,\*</sup>

<sup>a</sup> School of Materials Science and Engineering, Ocean University of China, Qingdao 266100, China

<sup>b</sup> Qingdao Key Laboratory of Functional Membrane Material and Membrane Technology, Qingdao Institute of Bioenergy and Bioprocess Technology, Chinese Academy of Sciences, Qingdao 266101, China

<sup>c</sup> State Key Laboratory of Rare Earth Resource Utilization, Changchun Institute of Applied Chemistry, Chinese Academy of Sciences, Changchun 130022, China

<sup>d</sup> Department of Materials Science and Engineering, Southern University of Science and Technology, Shenzhen 518055, China

<sup>e</sup> School of Physics and Astronomy, University of Birmingham, Birmingham B15 2TT, UK

## ARTICLE INFO

### Keywords:

Ru single atoms  
Ultrafine nanoclusters  
Strong electronic coupling effect  
Hydrogen evolution reaction  
Economical catalyst

## ABSTRACT

Although Ru-based materials have been recognized as promising electrocatalysts for hydrogen evolution reaction (HER), further improving the mass activity and guaranteeing the high-throughput H<sub>2</sub> production of the catalysts is of vital importance. Herein, Ru single atoms coupling with ultrafine nanoclusters on hierarchical porous N-doped carbon (NMC-Ru<sub>SA+NC</sub>) has been synthesized as economical and effective HER catalysts. Density function theory and the experimental results reveal that the strong electronic coupling effects between Ru single atoms and nanoclusters and unique hierarchical structure enable NMC-Ru<sub>SA+NC</sub> with the ultralow overpotential for achieving 500 mA cm<sup>-2</sup> in alkaline and acidic conditions. More importantly, the NMC-Ru<sub>SA+NC</sub> affords a higher mass activity and a lower cost for generating H<sub>2</sub> than those of commercial Pt/C, justifiably proving its remarkable advantages for industrial use. This work offers precise guidance to design catalysts for high-throughput H<sub>2</sub> production from the in-depth understanding of the electronic coupling effect of coupling active sites.

## 1. Introduction

Hydrogen, an ideal energy carrier with high energy density (~ 142 MJ kg<sup>-1</sup>) and zero-emission, has received much interest as a viable substitute for traditional fossil fuels in the face of intensifying severe energy crises and environmental pollution [1–4]. Water electrolysis with satisfactory efficiency and high product purity is generally regarded as the promising and environmentally friendly technology to produce green hydrogen [5–7]. Hydrogen evolution reaction (HER) as a half-reaction frequently suffers from sluggish kinetics owing to its complex elementary reaction steps (Volmer-Heyrovsky or Volmer-Tafel pathway), and thus cost-effective electrocatalysts are highly needed to accelerate the HER process [8–10]. Pt-based materials are still the most efficient catalysts and afford the unparalleled activities for HER, but their nature scarcity and high cost (~988 \$ per oz) cause the catalysts price to rise, accounting for 8% of the cost of the practical electrolyzer stack [11–15]. Tremendous efforts have been devoted to decreasing the

catalysts price by substituting Pt in the design of the catalyst. Ru element is considered as the promising alternative in view of Pt-like bond strength with hydrogen (~ 65 kcal mol<sup>-1</sup>) and the lowest price among non-platinum noble metals (42 \$ per oz, Table S1) [16–22]. It has been reported that Ru-based catalysts with high loading possess comparable HER activities to Pt. In these cases, their atom utilization efficiency is significantly limited as Ru atoms are easily agglomerated into large nanoparticles driven by their large cohesive energy, thus resulting in unsatisfactory mass activities [23–27]. As is well known, the reduction of Ru loading has been proposed as one of the effective strategies to maximize the atoms utilization efficiency. Nevertheless, it has met with much less success in simultaneously achieving the high mass activity and guaranteeing the high-throughput H<sub>2</sub> production of these catalysts.

The challenges encountered in the complicated HER are manifold, such as the intrinsic activities of catalysts, accessible active sites, and the effective removal of generated H<sub>2</sub> from the active sites [1,28,29]. The decrease of Ru loading would frequently result in the low density of

\* Corresponding authors.

E-mail addresses: [huangminghua@ouc.edu.cn](mailto:huangminghua@ouc.edu.cn) (M. Huang), [jianghq@qibebt.ac.cn](mailto:jianghq@qibebt.ac.cn) (H. Jiang).

<sup>1</sup> These authors contributed equally to this work.

active sites, which is detrimental to the realization of the economical and effective high-throughput  $H_2$  production [25,30,31]. Therefore, it remains a priority to achieve a high reaction rate for the active sites, which in turn requires the accelerated reaction kinetics of the active sites, the rapid transport of the intermediates and the timely release of the formed  $H_2$  bubbles. Two important factors should be thus considered - the fast reaction kinetics and optimized mass transfer capacity in the electrochemical HER process [32–35]. To begin with, construction of the multi-coupling active sites has been surfaced as an effective way to facilitate the HER kinetics [23,25,36,37]. For instance, Chen's group synthesized the Ru single atoms (SAs) and nanoparticles (NPs) loaded on the carbon nanowires, which exhibited an overpotential of 12 mV at the current density of  $10 \text{ mA cm}^{-2}$ . The excellent HER activity was dominantly ascribed to the existence of Ru SAs, accompanied with the minimal contributions from the Ru NPs [36]. Liu et al. fabricated the coupling Ru SAs and NPs sites on the defective carbon, in which the former could effectively improve the adsorption free energy of  $H^*$  and the latter could significantly reduce the energy barrier of water dissociation (Volmer reaction step). Such multi-coupling active sites enable the catalysts with the superior HER activities in acidic and alkaline media [25]. Unfortunately, most of the mentioned fascinating endeavors can only operate at the limited current density of less than  $200 \text{ mA cm}^{-2}$ , which would be harmful to achieving the high-throughput  $H_2$  production. The current densities needed for industry practical application are usually higher than  $500 \text{ mA cm}^{-2}$  [38]. In this regard, the mass transport capacity is another important factor for the successful construction of efficient HER catalysts. It has been demonstrated that hierarchical porous architecture with a large accessible surface area and numerous mass transport channels could be beneficial to facilitating the rapid transport of the reactants to, and removal of the produced  $H_2$  from, these active sites, thus boosting the HER performance at large current densities [25,39–41]. According to the aforementioned analysis, the economical and effective catalysts are thus required to include the multi-coupling active sites for realizing the fast reaction kinetics, while simultaneously possessing the hierarchical porous architecture to allow the rapid reactants transport and the timely  $H_2$  removal for achieving the superior performance at large current densities, but it is rarely reported to date.

Herein, we deliberately design and fabricate Ru single atoms coupling with ultrafine nanoclusters anchored on hierarchical porous N-doped carbon (NMC-Ru<sub>SA+NC</sub>), which could serve as economical and effective HER catalysts at high current densities in both alkaline and acidic conditions. Theoretical calculations and the experimental analysis reveal that the coupling Ru single atoms and nanoclusters could cooperate with each other and produce the strong electronic coupling effects, which could be beneficial to achieving the fast water dissociation and optimized metal-adsorbate  $H^*$  strength. Furthermore, the hierarchical porous structure could effectively speed up the rapid transport of the reactants and timely  $H_2$  removal, thus endowing the NMC-Ru<sub>SA+NC</sub> with a ultralow overpotential of 185, 161 mV at a high current density of  $500 \text{ mA cm}^{-2}$  in 1.0 M KOH and 0.5 M  $H_2SO_4$ , respectively. Moreover, the NMC-Ru<sub>SA+NC</sub> possesses the higher mass activity and turnover frequency value than those of Pt/C and other recently reported Ru-based HER electrocatalysts. Notably, the cost for generating per liter  $H_2$  is determined to be  $0.0028 \$ \text{ cm}^{-2} \text{ L}_{H_2}^{-1}$  for the NMC-Ru<sub>SA+NC</sub> in both alkaline and acidic conditions, 231 and 243 times lower than those of commercial Pt/C ( $0.648 \$ \text{ cm}^{-2} \text{ L}_{H_2}^{-1}$  in alkaline and  $0.680 \$ \text{ cm}^{-2} \text{ L}_{H_2}^{-1}$  in acidic condition), respectively. This work also provides a series of evaluation methods to investigate the practical applications of the catalysts. These results justifiably proved that the NMC-Ru<sub>SA+NC</sub> has remarkable advantages for industrial use because of its high  $H_2$  production rate and low catalyst price, which provides new insights and ideas for the research of hydrogen evolution catalysts in practical application.

## 2. Experimental section

### 2.1. Synthesis of N-doped mesoporous polymer (NMP)

Typically, 3-aminophenol (MAP, 3.8 mmol) and hexamethylenetetramine (HMT, 4.7 mmol) were first dissolved together in 75 mL deionized water under continuously stirring, followed by the addition of the aqueous solution of F127 (8.4% w/w%, 5 mL) to form the mixed solution. After undergoing stirring at  $50^\circ\text{C}$  for 16 h, the mixed aqueous solution was transferred into a Teflon-lined autoclave and reacted at  $130^\circ\text{C}$  for 8 h. Finally, the NMP powders were collected after centrifuging the mixture solution with deionized water for several times and freeze-drying.

### 2.2. Synthesis of ruthenium single atoms and ultrafine nanoclusters anchored on hierarchical N-doped mesoporous carbon catalyst (NMC-Ru<sub>SA+NC</sub>)

100 mg NMP was dissolved in deionized water under ultrasonication for 30 min and subsequently stirred for 30 min. After 1.5 mL  $RuCl_3$  solution (25.65 mM) was injected into the NMP solution at room temperature, the mixture was immediately transferred into low temperature environment and then placed for 24 h, followed by freeze-drying to obtain the precursor. Finally, the NMC-Ru<sub>SA+NC</sub> was obtained by pyrolyzing the precursor at  $700^\circ\text{C}$  for 3 h under  $N_2$  atmosphere with a heating rate of  $2^\circ\text{C min}^{-1}$ .

### 2.3. Synthesis of ruthenium nanoclusters anchored on carbon black catalyst (Ru/C)

100 mg carbon black (VC-72X) was dissolved in deionized water under ultrasonication for 30 min and subsequently stirred for 30 min. After 1.5 mL  $RuCl_3$  solution (25.65 mM) was injected into the above solution at room temperature, the mixture was immediately transferred into low temperature environment and then placed for 24 h, followed by freeze-drying to obtain the precursor. Finally, the Ru/C was obtained by pyrolyzing the precursor at  $700^\circ\text{C}$  for 3 h under  $N_2$  atmosphere with a heating rate of  $2^\circ\text{C min}^{-1}$ .

### 2.4. Synthesis of ruthenium single atoms anchored on hierarchical N-doped mesoporous carbon catalyst (NMC-Ru<sub>SA</sub>)

The NMC-Ru<sub>SA</sub> was synthesized by using the same procedure of the NMC-Ru<sub>SA+NC</sub> with the addition of 1.5 mL  $RuCl_3$  solution (1.28 mM).

### 2.5. Materials characterization

Transmission electron microscopy (TEM) were performed on a Hitachi H-7650 microscope operated at 120 kV. The high-resolution TEM (HRTEM), high angle annular dark field scanning transmission electron microscopy (HAADF-STEM) and energy-dispersive X-ray spectroscopy (EDS) elemental mapping were performed on a JEM-2100 F microscope operated at 120 kV. The aberration-corrected HAADF-STEM was taken on Titan Cubed Themis G2 300. XRD patterns were collected on a Bruker D8 Advance diffractometer. Raman spectroscopy was measured on a Thermo Fisher spectrometer equipped with 532 nm argon lasers and 633 nm helium-neon. X-ray photoelectron spectroscopy (XPS) was carried out on a Thermo ESCALAB 250XI. The content of Ru metal was measured by inductively coupled plasma-optical emission spectrometry (ICP-OES). The specific surface area and pore sizes were investigated by using the Brunauer-Emmett-Teller (BET) and Barrett-Joyner-Halenda (BJH) method, respectively. The X-ray absorption spectra (XAS) including X-ray absorption near-edge structure (XANES) and extended X-ray absorption fine structure (EXAFS) at Ru K-edge of the samples were measured at the beamline 14 W of Shanghai Synchrotron Radiation Facility (SSRF) in China. The contact angles (CAs) of

the NMC-Ru<sub>SA+NC</sub> and the Pt/C were tested at room temperature. Each contact angle measurement was repeated at least four times.

## 2.6. Electrochemical measurements

Electrochemical measurements were performed on an electrochemical workstation (CHI-660E) in a conventional three-electrode system at room temperature. The HER activity testing was performed by linear sweep voltammetry (LSV) at a scan rate of 5 mV s<sup>-1</sup> with 100%-iR compensation. Electrochemical impedance spectroscopy (EIS) was carried out at an overpotential of 30 mV from 10 kHz to 0.1 Hz. The long-term stability tests were carried out by chronopotentiometric measurements without iR compensation. The detailed electrochemical measurements section and the calculation details section can be found in the [supporting information](#).

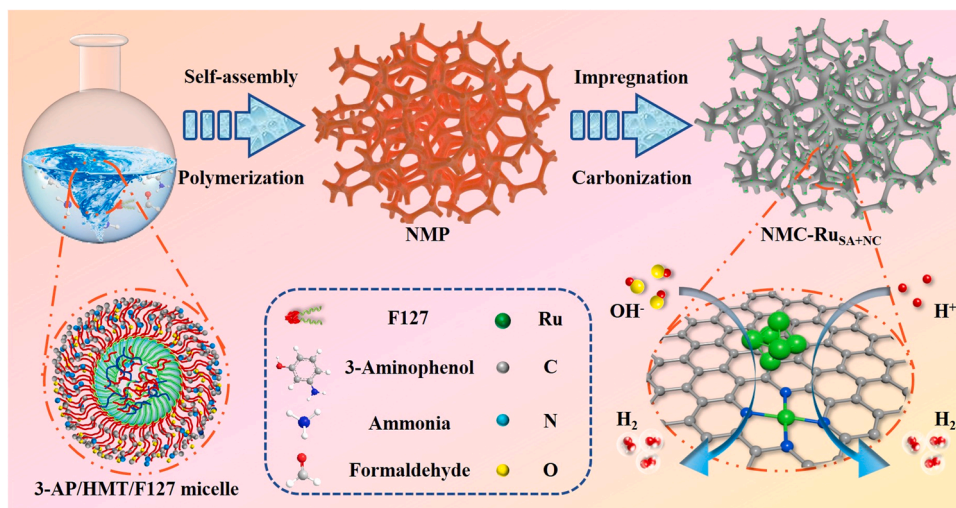
## 3. Results and discussion

### 3.1. Morphology and structure characterization of catalysts

The overall synthetic route of the NMC-Ru<sub>SA+NC</sub> is schematically summarized in [Scheme 1](#). The NMP was first synthesized using the soft-template strategy, followed by the introduction of Ru<sup>3+</sup> and subsequent thermal reduction to obtain the NMC-Ru<sub>SA+NC</sub> with both single Ru atoms and ultrafine Ru nanoclusters. In addition, the control catalysts with only Ru nanoclusters (denoted as Ru/C) and only Ru single atoms (denoted as NMC-Ru<sub>SA</sub>) were prepared for comparison, respectively. Transmission electron microscopy (TEM) was used to investigate the detailed morphology structures of the NMC-Ru<sub>SA+NC</sub>. As shown in [Fig. 1a](#), the NMC-Ru<sub>SA+NC</sub> displays the highly interconnected hierarchical network with multi-dimensional macro/meso/microporous structures, which well maintains the original morphology of the NMC ([Fig. S1](#)). Such unique structure could not only be used as “high-ways” to accelerate the collision between the active sites and electrolyte, but also provide enough space to guide the effective release of the generated gas bubbles, and thus be beneficial to achieving the fast mass transfer for the improvement of the HER performance.[\[39\]](#) As shown in [Fig. 1b](#) and [c](#), ultrafine nanoclusters with an average diameter of about 3.5 nm are observed to be homogeneously dispersed on the carbon skeleton. The high-resolution TEM (HRTEM) images show ([Fig. 1d–f](#)) that the lattice fringe spacings are determined to be 0.214 nm, 0.206 nm and 0.234 nm, which can be well ascribed to the (002), (101) and (100) planes of Ru nanoclusters, respectively, as also evidenced by the selected area electron diffraction (SAED, [Fig. S2](#)) and X-ray diffraction (XRD) patterns

([Fig. S3](#)). The high angle annular dark-field scanning TEM (HAADF-STEM) and elemental mapping images ([Fig. 1g](#) and [h](#)) display that the NMC-Ru<sub>SA+NC</sub> consists of C, N, and Ru elements. The aberration-corrected (AC) HAADF-STEM images ([Fig. 1i](#) and [S4](#)) further demonstrate the existence of the Ru nanoclusters in the NMC-Ru<sub>SA+NC</sub>. More interestingly, a number of single bright dots corresponding to Ru atoms are homogeneously dispersed on the carbon framework. It is noting that some of single Ru atoms marked by red circles are situated as the neighbors around the Ru nanoclusters ([Fig. 1j](#)), which could be advantageous to producing the strong coupling effect between them for boosting the catalytic HER activities [\[42,43\]](#). The Ru content is determined to 2.0 wt% for the NMC-Ru<sub>SA+NC</sub> by inductively coupled plasma-optical emission spectrometer (ICP-OES). For the NMC-Ru<sub>SA</sub>, no distinct signals indexing the Ru clusters can be captured in XRD patterns and TEM images ([Fig. S3](#) and [S5a,b](#)), implying that the Ru might exist in a form of single atoms in the NMC-Ru<sub>SA</sub> catalyst. As shown in [Fig. S5c](#) and [d](#), it can be clearly seen from the AC HAADF-STEM images that some single Ru atoms as brighter dots are uniformly distributed within the NMC framework, evidently demonstrating that the NMC-Ru<sub>SA</sub> is composed exclusively of Ru single atoms. For the Ru/C with the Ru content of 2.8 wt% (determined by ICP-OES), the obvious signals indexing the Ru nanoclusters can be readily captured in XRD patterns, TEM, and HRTEM images ([Figs. S3](#) and [S6](#)), and no single Ru atoms can be identified in the AC-HAADF-STEM images for the Ru/C ([Fig. S7](#)), indicating that the Ru/C consists exclusively of Ru nanoclusters.

X-ray photoelectron spectroscopy (XPS) was conducted to investigate the chemical state of the NMC, NMC-Ru<sub>SA+NC</sub> and Ru/C ([Figs. 2a](#) and [S8](#)). Signal for the C, N, O and Ru elements are clearly captured in the XPS survey spectrum of the NMC-Ru<sub>SA+NC</sub>. As shown in [Fig. 2b](#), the Ru 3p XPS spectrum is divided into four peaks attributing to metallic Ru (ca. 462.7 and 485.3 eV) and Ru<sup>n+</sup> species (ca. 466.7 and 490.0 eV), respectively.[\[23,40,44\]](#) It can be seen in [Table S2](#) that the metallic Ru species and Ru<sup>n+</sup> species for the NMC-Ru<sub>SA+NC</sub> account for 73.1% and 26.9% of the total Ru content. Meanwhile, the Ru-N bond at ca. 399.2 eV can be found in the high-resolution N 1 s spectrum ([Figs. 2c](#), [S9](#), [S10](#) and [Table S3](#)) [\[23\]](#). These results indicate the co-existence of Ru nanoclusters and atomically dispersed RuN<sub>x</sub> sites in NMC-Ru<sub>SA+NC</sub>. Only two peaks indexing metallic Ru species can be observed at ca. 462.4 and 484.9 eV in the Ru 3p spectrum for the Ru/C ([Fig. S11](#)). Interestingly, a positive binding energy shift of ca. 0.3 eV for the metallic Ru species can be captured on the NMC-Ru<sub>SA+NC</sub> compared with the Ru/C, indicating the electron transfer from Ru nanoclusters to atomically dispersed Ru-N<sub>x</sub> sites, which could be conducive to producing the strong electronic coupling effects for enhancing the catalytic HER activities [\[31,45\]](#).



**Scheme 1.** Schematic representation of the synthetic process for the NMC-Ru<sub>SA+NC</sub>.

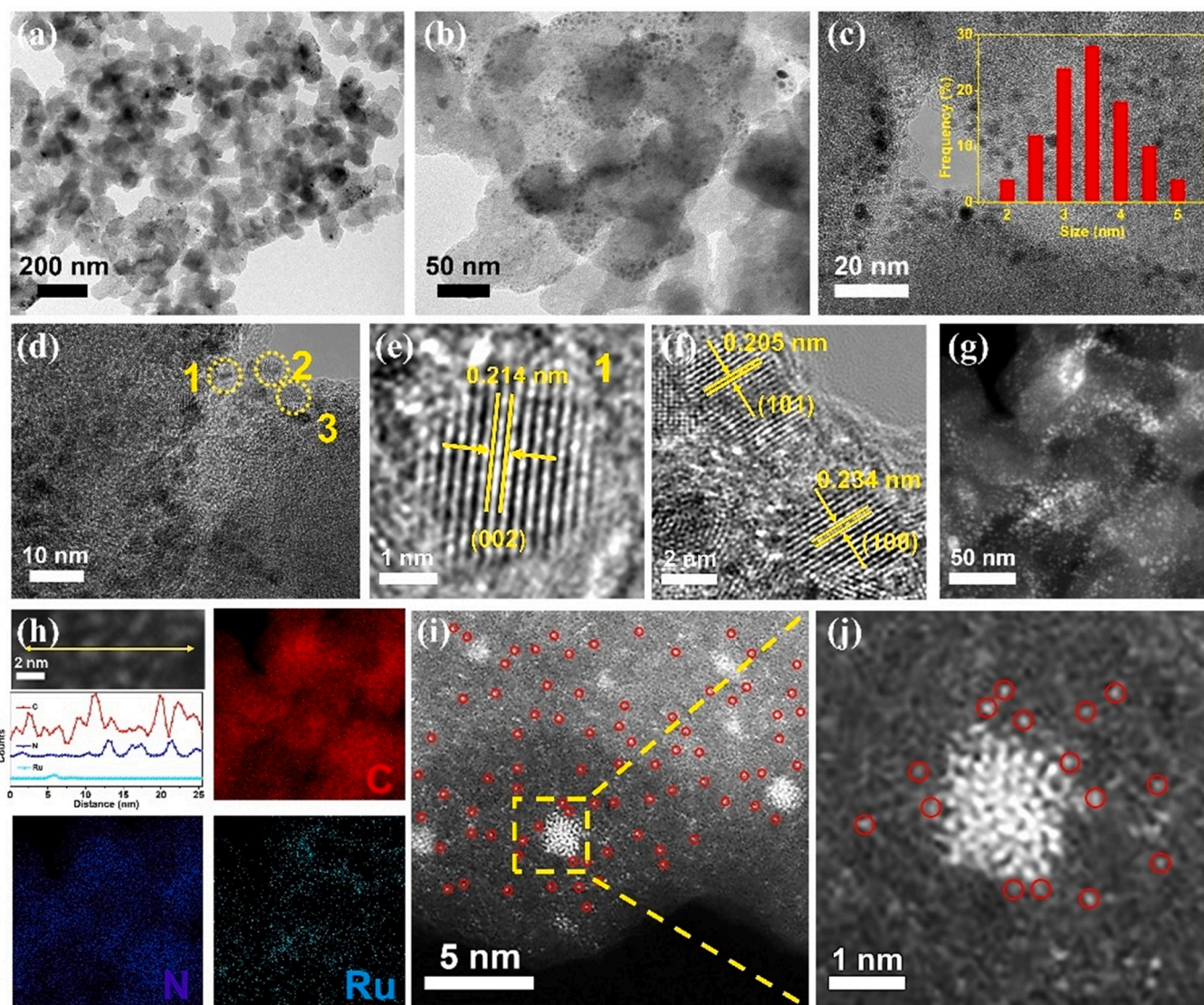


**Fig. 1.** (a, b) TEM images, (c-f) HRTEM images. The inset in (c) shows the size distribution of Ru nanoclusters. (g, h) HAADF-STEM images and corresponding element mapping images of C, N and Ru elements in NMC-Ru<sub>SA+NC</sub>. (i, j) AC-HAADF-STEM images of the NMC-Ru<sub>SA+NC</sub> (atomic Ru species circled by red).

X-ray absorption fine structure (XAFS) measurements at Ru K-edge, including X-ray absorption near-edge structure (XANES) and extended X-ray absorption fine structure (EXAFS) spectroscopies, were also performed to obtain the coordination information of the NMC-Ru<sub>SA+NC</sub> accompanied with the Ru foil and RuO<sub>2</sub> as the reference (Fig. 2d and e). It can be seen in XANES spectrum that K-edge position of Ru in the NMC-Ru<sub>SA+NC</sub> is located between the Ru foil and RuO<sub>2</sub> (Fig. 2d), indicating that the average valence state of Ru element is between 0 and +4. Fig. 2e shows the Fourier transformed (FT) EXAFS spectrum of the NMC-Ru<sub>SA+NC</sub>. The peak located at 1.5 Å could be ascribed to the Ru-N/O bond of the single Ru atom coordinated with N/O, whereas the peak at about 2.2 Å could be assigned to Ru-Ru bond of the Ru nanoclusters. As shown in the Wavelet transformed (WT) EXAFS spectrum of the NMC-Ru<sub>SA+NC</sub> (Fig. 2f), the obvious signals at 5.4 and 9.4 Å<sup>-1</sup> correspond to the Ru-N/O and Ru-Ru bond, respectively. Further support for the existence of these bonds can be provided by the k-space EXAFS fitting (Fig. 2g), suggesting the formation of single Ru atoms and Ru nanoclusters in the NMC-Ru<sub>SA+NC</sub>. The EXAFS fitting in R-space reveals that the coordination number of Ru-N is determined to be 3.5 (close to 4), indicating that the single Ru atoms exist in a form of RuN<sub>4</sub> structure for the NMC-Ru<sub>SA+NC</sub> (Table S4).

To gain insight into the porous characteristics of materials, the

nitrogen (N<sub>2</sub>) adsorption-desorption isotherm were recorded to investigate the surface area and pore size distribution of the obtained catalysts. As displayed in Fig. S12a, typical type-IV isotherms with the evident hysteresis loops are observed for the NMC and NMC-Ru<sub>SA+NC</sub>, featuring their mesoporous nature. While the rapidly decreased N<sub>2</sub> uptake at low relative pressure (< 0.1) indicates the presence of the micropores (< 2 nm), the sharply increased N<sub>2</sub> uptake at a high relative pressure (> 0.9) suggests the existence of abundant macropores (> 50 nm). The pore size distribution curves in Fig. S12b further manifest the formation of hierarchical macro/meso/microporous structures, in accordance with the above TEM analysis. Benefiting from the plentiful hierarchical porous structures, the NMC-Ru<sub>SA+NC</sub> exhibits a large surface area of 547.3 m<sup>2</sup> g<sup>-1</sup> and a high pore volume of 1.05 cm<sup>3</sup> g<sup>-1</sup>, which could effectively promote exposure of more active sites and rapid mass transport of reactants, thus achieving the boosted HER performance. Raman spectra in Fig. S13 display two typical signals at ca. 1335 and 1595 cm<sup>-1</sup>, which are indexed to the characteristic D and G bands of the carbon, respectively [46]. Noted that the NMC-Ru<sub>SA+NC</sub> affords a lower intensity ratio of D to G bands (1.28) than the NMC-Ru<sub>SA</sub> (1.34), NMC (1.58) and Ru/C (1.32), indicating that the introduction of Ru could increase the graphitization degree of the carbon framework, which is expected to be of high interest for enhancing the electron

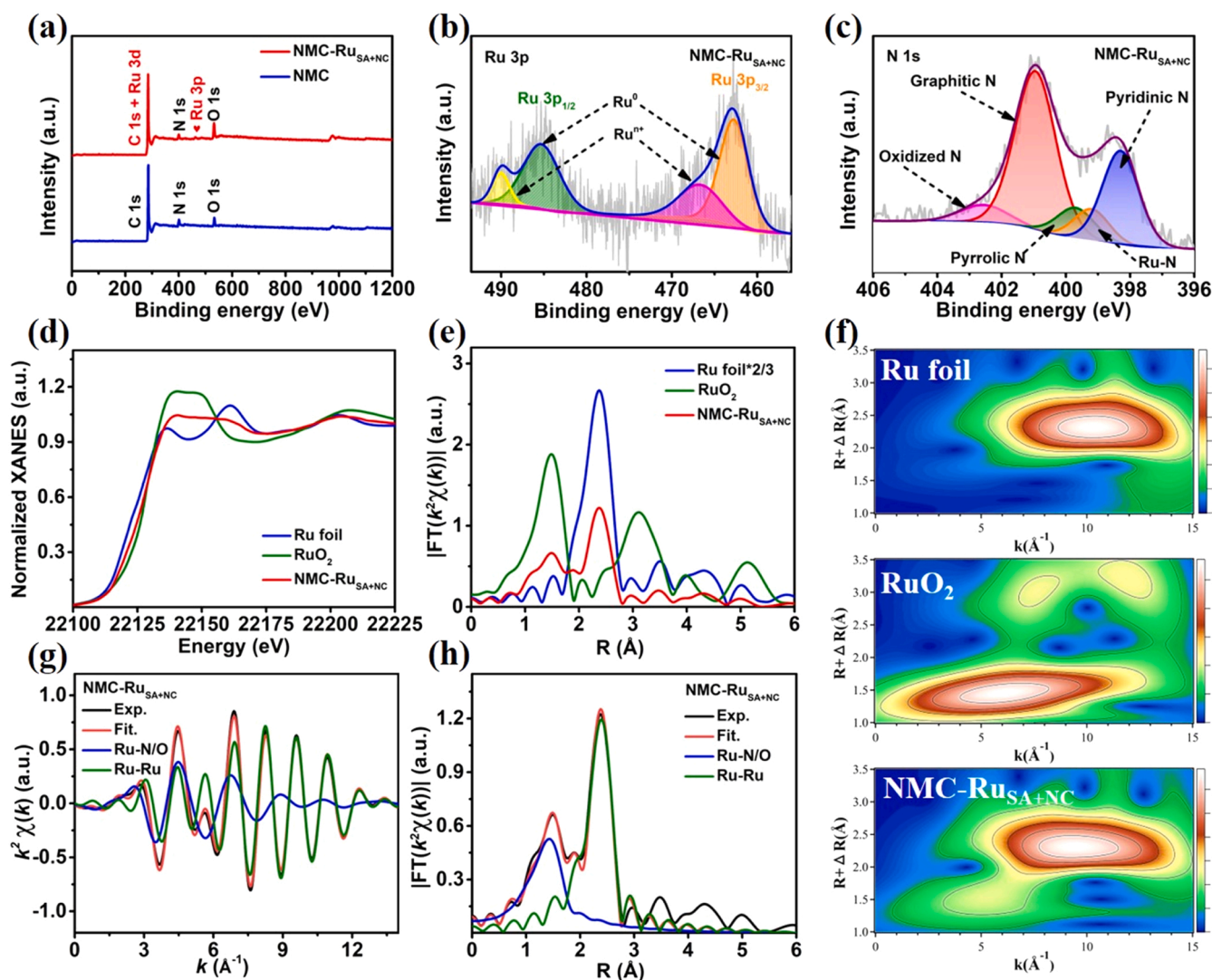


**Fig. 2.** (a) XPS survey spectra of the NMC-Ru<sub>SA+NC</sub> and NMC. (b) Ru 3p and (c) N 1s high-resolution XPS spectra of the NMC-Ru<sub>SA+NC</sub>. (d) XANES spectra, (e) FT-EXAFS spectrum and (f) Wavelet transforms (WT) contour plots of Ru foil, RuO<sub>2</sub> and NMC-Ru<sub>SA+NC</sub>. FT-EXAFS fitting curves in (g) k space and (h) R space for the NMC-Ru<sub>SA+NC</sub>.

transfer for achieving the efficient HER.

### 3.2. Evaluation of HER performance in alkaline solution

Inspired by the above-mentioned features, the NMC-Ru<sub>SA+NC</sub> with both single Ru atoms and ultrafine Ru nanoclusters is anticipated to possess excellent catalytic HER activity, which is first evaluated in 1 M KOH by a typical three-electrode system. As depicted by the linear sweep voltammetry (LSV) curves in Fig. 3a, the NMC-Ru<sub>SA+NC</sub> only needs the overpotential ( $\eta$ ) of 5 mV to achieve the current density of 10 mA cm<sup>-2</sup> ( $j_{10}$ ), which is lower than that of the NMC, NMC-Ru<sub>SA</sub>, Ru/C and Pt/C catalysts. Compared with the Pt/C, NMC-Ru<sub>SA</sub>, and Ru/C, the lower overpotentials of the NMC-Ru<sub>SA+NC</sub> at the all investigated current densities ( $j = 20, 50, 100, 200$  and 500 mA cm<sup>-2</sup>) also confirm its advanced HER catalytic activity, which can be more remarkably highlighted at high current density (Figs. 3a and S14). As shown in Fig. 3b, the Tafel slope of the NMC-Ru<sub>SA+NC</sub> is calculated to be 55 mV dec<sup>-1</sup>, suggesting that the HER pathway is controlled by desorption of H\* via a typical Volmer-Heyrovsky mechanism that is schematically presented in Fig. 3c. [47,48] The Ru/C with only Ru nanoclusters owns a Tafel slope of 136 mV dec<sup>-1</sup> (Fig. 3b), indicating that the rate-determining step (RDS) is controlled by the water dissociation step ( $\text{H}_2\text{O} + \text{e}^- \rightarrow \text{H}_{\text{ads}} + \text{OH}^-$ )

[49]. The difference in the Tafel slope between the above two catalysts indicates that the existence of the single Ru atoms in the NMC-Ru<sub>SA+NC</sub> could be advantageous to facilitating the water dissociation step. To deeply investigate the contributions of single Ru atoms and Ru nanoclusters toward catalyzing HER, the poisoning experiments were adopted by using EDTA and SCN<sup>-</sup> as the complexing reagents, in which EDTA could dominantly coordinate with the single Ru atoms and SCN<sup>-</sup> would complex with both the single Ru atoms and Ru nanoclusters for retarding their HER activities [36,42,50]. As shown in Fig. S15, the negative shift of overpotential (240 mV) after the addition of SCN<sup>-</sup> is higher than that after the addition of EDTA (50 mV), implying that both single Ru atoms and Ru nanoclusters contribute to the excellent HER activities for the NMC-Ru<sub>SA+NC</sub>. Interestingly, the Tafel slope was decreased from 55 to 128 mV dec<sup>-1</sup> accompanied with the addition of EDTA for poisoning single Ru atoms, indicating the RDS is changed to be the water dissociation step, which further decodes the existence of single Ru atoms could accelerate the water dissociation step (Fig. S16). By contrast, the overpotential of the Ru/C displays the negligible change after the introduction of EDTA, and the shift of overpotential is ~180 mV after the addition of SCN<sup>-</sup> (Fig. S15). Taken together, one may conclude that single Ru atoms and Ru nanoclusters could cooperate with each other and produce the strong electronic coupling effect to achieve

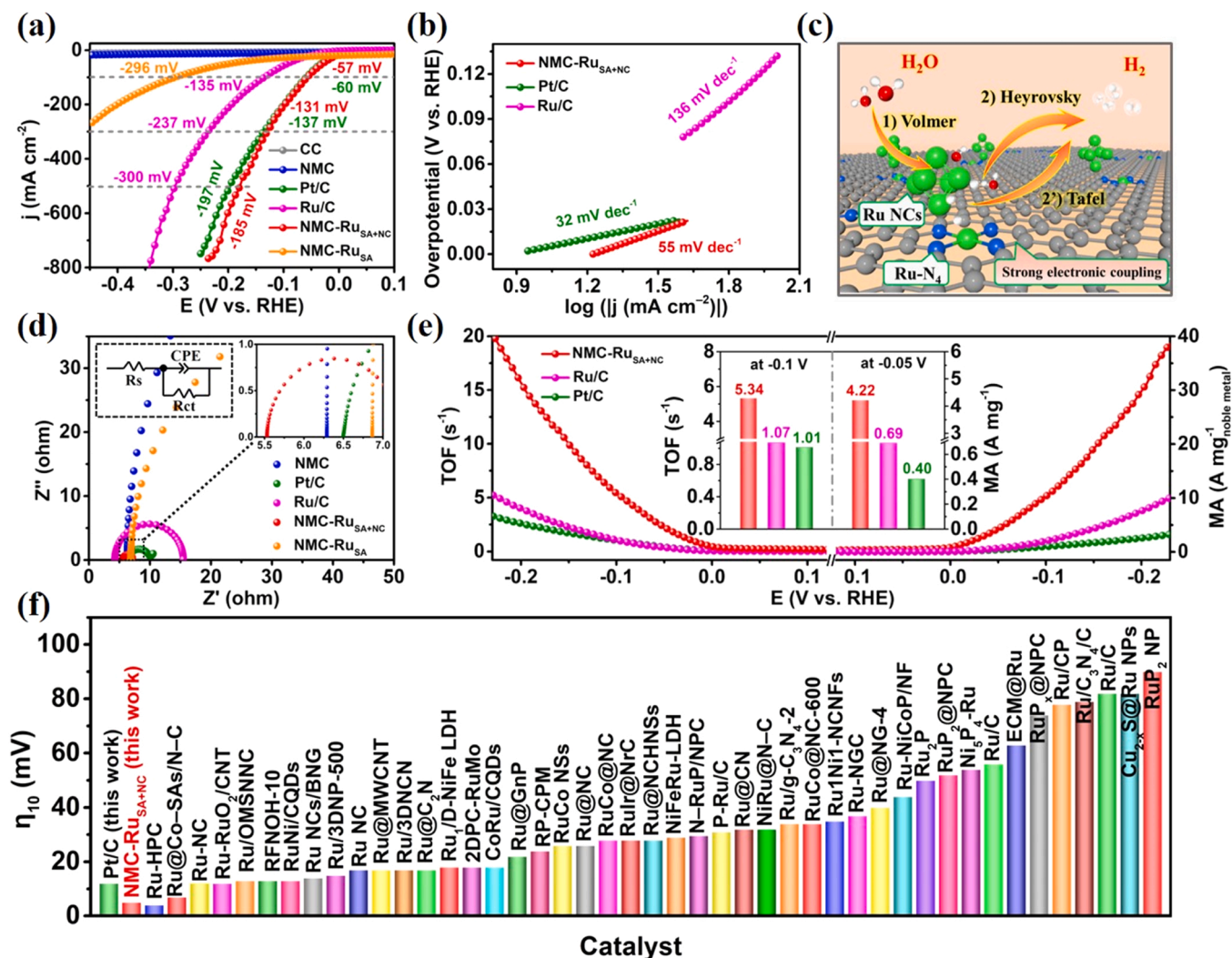


**Fig. 3.** (a) LSV curves of the NMC-Ru<sub>SA+NC</sub> and the control catalysts in 1.0 M KOH. (b) Tafel plots of the NMC-Ru<sub>SA+NC</sub>, Ru/C and commercial Pt/C, (c) the corresponding HER mechanism. (d) Nyquist plots of as-prepared materials (inset: the enlarged EIS curves). (e) Turnover frequency and mass activity of the NMC-Ru<sub>SA+NC</sub>, Ru/C and commercial Pt/C. (f) The comparison of overpotentials for the NMC-Ru<sub>SA+NC</sub> with other recently reported HER electrocatalysts at 10 mA cm<sup>-2</sup> in 1 M KOH solution.

the enhanced HER activities for the NMC-Ru<sub>SA+NC</sub>, in which the former plays a key role on accelerating the water dissociation step.

To explore the electrochemical active surface area (ECSA) of the catalysts, the double layer capacitances ( $C_{dl}$ ) were calculated from CV curves operated in a non-Faradaic potential region. As shown in Fig. S17, the NMC-Ru<sub>SA+NC</sub> displays the highest  $C_{dl}$  (34.5 mF cm<sup>-2</sup>) among all the investigated catalysts, indicating a remarkably increased number of accessible active sites after the introduction of single Ru atoms and Ru nanoclusters on the carbon skeleton. The ECSA-normalized LSV curves in Fig. S18 display that the NMC-Ru<sub>SA+NC</sub> affords the higher specific activity than the control catalysts, which is comparable to that of the commercial Pt/C, indicating the coupling Ru single atoms and Ru nanoclusters enables the catalysts with high specific activity in alkaline solution. The Nyquist plots derived from electrochemical impedance spectroscopy (EIS, Fig. 3d) indicate that the NMC-Ru<sub>SA+NC</sub> possesses the smallest charge transfer resistance among all the investigated catalysts, manifesting the superior electron transfer and reaction kinetics. The long-term stability, another essential parameter to assess electrochemical performance in practical application, was investigated by the chronopotentiometric measurements employed at the current density of 50 mA cm<sup>-2</sup> (Fig. S19). The NMC-Ru<sub>SA+NC</sub> exhibits the good long-term durability that could operate over 100 h, which is

comparable to that of the commercial Pt/C. The multi-step chronopotentiometric measurements for the NMC-Ru<sub>SA+NC</sub> were performed from 100 to 600 mA cm<sup>-2</sup> and followed by returning to 100 mA cm<sup>-2</sup>, where no significant change can be detected in the potential of each stage (Fig. S20). Notably, only a 5.7% increase of the potential was captured when the current density is back to 100 mA cm<sup>-2</sup>, further suggesting the striking mechanical robustness and good reversibility at the high current density for the NMC-Ru<sub>SA+NC</sub>. TEM and XPS were employed to investigate the structure and morphology for the NMC-Ru<sub>SA+NC</sub> after the long-term stability test. As shown in Fig. S21a, the NMC-Ru<sub>SA+NC</sub> maintains the original morphologies after the stability test in alkaline solution. Fig. S21b displays the corresponding Ru 3p XPS spectra of NMC-Ru<sub>SA+NC</sub> after the long-term stability, in which four peaks attributing to metallic Ru (ca. 462.7 and 485.3 eV) and Ru<sup>n+</sup> species (ca. 466.7 and 490.0 eV) can be captured. It can be seen in Table S2 that the relative content of metallic Ru species increased to 74.4%, whereas the relative content of Ru<sup>n+</sup> species decreased to 25.6%, indicating that the Ru species were slightly agglomerated during the catalytic process in alkaline solution. These results demonstrate the robust catalytic HER stability of the NMC-Ru<sub>SA+NC</sub> in alkaline solution.

Turnover frequency (TOF) was calculated by assuming all-metal Ru atoms as the active sites that could participate in catalyzing HER, which

serves as the key parameter to evaluate the inherent catalytic efficiency [51]. Fig. 3e shows that the TOF of the NMC-Ru<sub>SA+NC</sub> at the overpotential of 100 mV is determined to be 5.34 s<sup>-1</sup>, which is 5.0 and 5.28 folds than that of the Ru/C (1.07 s<sup>-1</sup>) and commercial Pt/C (1.01 s<sup>-1</sup>), respectively, verifying the exceptional activity of the NMC-Ru<sub>SA+NC</sub> toward HER. The mass activity (MA) is a significant quantitative factor to demonstrate the practical application of the NMC-Ru<sub>SA+NC</sub> since it determines the cost of catalysts. As shown in Fig. 3e, the NMC-Ru<sub>SA+NC</sub> exhibits a higher MA (4.22 A mg<sub>Ru</sub><sup>-1</sup>) than Ru/C (0.69 A mg<sub>Ru</sub><sup>-1</sup>) and Pt/C (0.40 A mg<sub>Pt</sub><sup>-1</sup>) at the overpotential of 50 mV, which even exceeds most of HER catalyst reported previously (Table S5), indicating the high utilization of Ru and the good economic competitiveness of the NMC-Ru<sub>SA+NC</sub>. Furthermore, the NMC-Ru<sub>SA+NC</sub> exhibits comparable HER overpotential to Ru-based catalyst reported in the previous literatures (Fig. 3f; Table S6). In consideration of the impressive catalytic activity and good stability, as well as the high inherent catalytic efficiency, it is sufficiently reasonable to state that the NMC-Ru<sub>SA+NC</sub> has a great potential to be a viable alternative to the Pt/C for practical applications in water splitting.

### 3.3. Evaluation of HER performance in acidic solution

Interestingly, the NMC-Ru<sub>SA+NC</sub> also exhibits excellent HER performance in an acidic environment (0.5 M H<sub>2</sub>SO<sub>4</sub>). As shown in the LSV curves (Fig. 4a), the NMC-Ru<sub>SA+NC</sub> requires a comparable overpotential (16 mV) to that of commercial Pt/C (13 mV) for achieving the current density of 10 mA cm<sup>-2</sup>, which is superior to that of NMC-Ru<sub>SA</sub> (133 mV) and Ru/C (46 mV) catalysts. When the current densities increase from 10 to 300 mA cm<sup>-2</sup>, the  $\eta$  of the NMC-Ru<sub>SA+NC</sub> is slightly larger than that of the Pt/C, but the gap is getting more narrower, or even disappears. It is worth noting that, at the large current densities (> 300 mA cm<sup>-2</sup>), the NMC-Ru<sub>SA+NC</sub> needs a smaller  $\eta$  than the Pt/C to achieve the same current densities. The overpotential of 161 mV is desired to reach up to 500 mA cm<sup>-2</sup> for the NMC-Ru<sub>SA+NC</sub>, whereas the Pt/C and Ru/C require the overpotential of 215 mV and 252 mV, respectively, indicating the superior HER performance for the NMC-Ru<sub>SA+NC</sub> at high current densities (Figs. 4a, and S22). It is possible that the single Ru atoms and ultrafine Ru nanoclusters on the hierarchical pores carbon framework could simultaneously provide more active center to catalyze HER and accelerate the collision between the electrolyte and active sites, thus achieving the rapid mass transfer to obtain the low  $\eta$  especially at the large current densities. As shown in Fig. 4b,

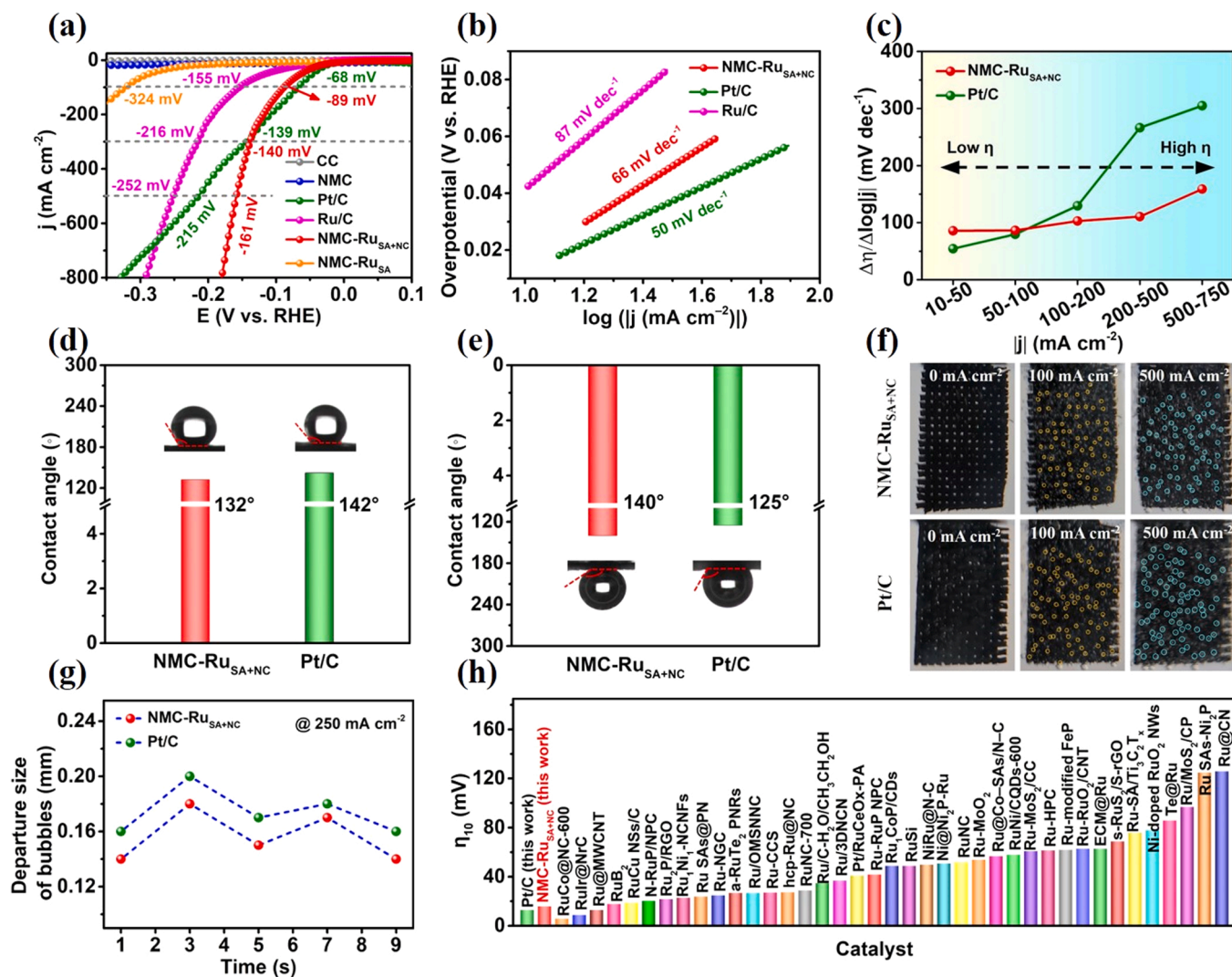


**Fig. 4.** (a) LSV curves of the NMC-Ru<sub>SA+NC</sub> and the control catalysts in 0.5 M H<sub>2</sub>SO<sub>4</sub>, (b) Tafel plots and (c) the  $\Delta\eta/\Delta\log|j|$  ratio of the NMC-Ru<sub>SA+NC</sub> and Pt/C catalysts. (d) Contact angles of electrolyte droplet and (e) contact angles of a H<sub>2</sub> bubble on the catalyst surfaces. (f) Photos of H<sub>2</sub> bubbles leaving the surfaces of the NMC-Ru<sub>SA+NC</sub> and Pt/C. (g) Size distributions of H<sub>2</sub> bubbles on the surfaces of the NMC-Ru<sub>SA+NC</sub> and Pt/C at  $j = 250$  mA cm<sup>-2</sup>. (h) The comparison of overpotentials for the NMC-Ru<sub>SA+NC</sub> with other recently reported HER catalysts at 10 mA cm<sup>-2</sup> in 0.5 M H<sub>2</sub>SO<sub>4</sub> solution.

the Tafel slope of the NMC-Ru<sub>SA+NC</sub> was determined to be 66 mV dec<sup>-1</sup> in the region of low  $j$ , suggesting that it follows the Volmer-Heyrovsky mechanism in acidic media. In the regions of high  $j$  (Fig. S23), the Tafel slope is kept the same as that in the region of low  $j$ , further manifesting its fast mass transfer capacity. The relationships between the  $\Delta\eta/\Delta\log|j|$  ratio and  $|j|$ , widely utilized as the indicator to investigate the high-current-densities performance of the catalysts, were constructed for the NMC-Ru<sub>SA+NC</sub> and Pt/C (Fig. 4c) [14,33]. With the increase of  $j$ , a small  $\Delta\eta/\Delta\log|j|$  ratio of NMC-Ru<sub>SA+NC</sub> can be constantly kept and the  $\Delta\eta/\Delta\log|j|$  ratio of the Pt/C sharply increases, indicative of the remarkable HER performance of the NMC-Ru<sub>SA+NC</sub> at large  $j$ .

The electrolyte/bubble contact angle (CA) measurements were performed to well understand the rapid mass transfer for the NMC-Ru<sub>SA+NC</sub>. Fig. 4d discloses that NMC-Ru<sub>SA+NC</sub> affords a lower CA of 132° than the Pt/C (142°), manifesting its good hydrophilicity, which would be conducive to the collision between the liquid electrolyte and the active sites, thus improving the catalytic activity. The other important factor for achieving excellent mass transfer is the rapid removal of the

generated hydrogen bubbles from the surface of catalysts. In Fig. 4e, the CA of bubbles is 140° for the NMC-Ru<sub>SA+NC</sub>, which is larger than that of Pt/C (125°), indicating the better aerophobicity of the NMC-Ru<sub>SA+NC</sub>. Further support is provided by calculating the size distribution of released hydrogen bubbles on the catalysts (Fig. 4f). As the current density increases, the diameter of hydrogen bubbles on the NMC-Ru<sub>SA+NC</sub> is always smaller than that of the Pt/C, suggesting the fast removal of hydrogen bubbles from the NMC-Ru<sub>SA+NC</sub> surface. Meanwhile, the time-dependent (30 frames per second) transport of hydrogen bubbles on the NMC-Ru<sub>SA+NC</sub> and the Pt/C was also investigated at the current densities of 250 mA cm<sup>-2</sup> (Fig. 4g), again manifesting the smaller H<sub>2</sub> bubbles on the NMC-Ru<sub>SA+NC</sub> surface than that of the Pt/C. This would prevent the active sites from being covered by the gathering hydrogen bubbles and be beneficial to exposing the active sites to the surrounding electrolyte, thus improving the mass transfer ability for the enhanced HER activities.

As shown in Fig. S24, the NMC-Ru<sub>SA+NC</sub> possess a higher  $C_{dl}$  than the NMC, decoding that the introduction of Ru could create more

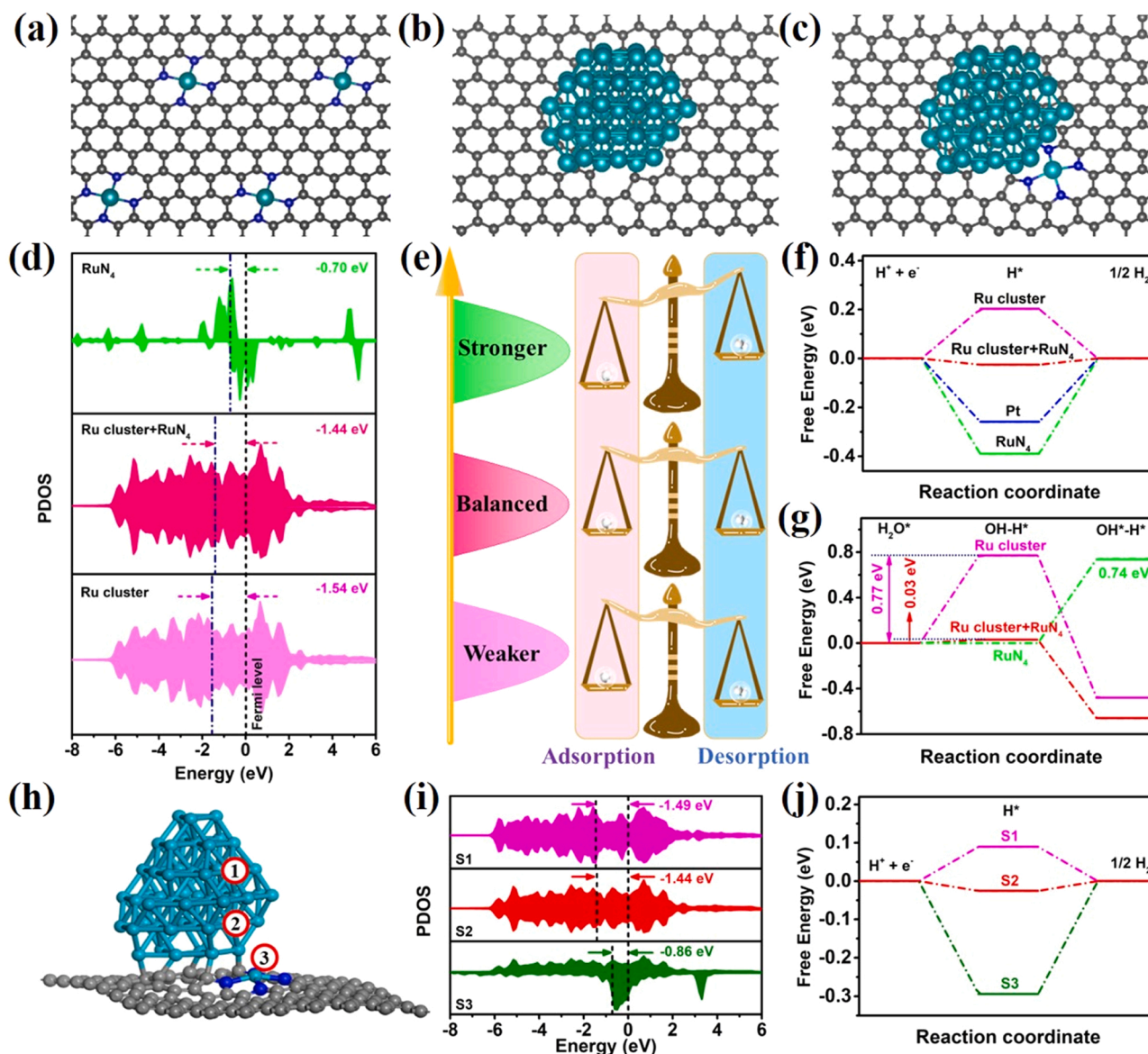


**Fig. 5.** Optimized structure models of (a) RuN<sub>4</sub>, (b) Ru cluster and (c) coupling Ru nanocluster+RuN<sub>4</sub> sites. (d) Projected density of states (PDOS) of Ru on the above three Ru systems. (e) Schematic illustration between the d band centers and adsorption-desorption abilities of HER intermediates. (f) Comparison of  $\Delta G_{H^+}$  of HER on RuN<sub>4</sub>, Ru cluster, Ru cluster+RuN<sub>4</sub> and Pt system. (g) The calculated energy barrier for water dissociation on RuN<sub>4</sub>, Ru cluster and Ru cluster+RuN<sub>4</sub> system. (h) Atomic configurations, (i) PDOS and (j)  $\Delta G_{H^+}$  of possible Ru active sites in Ru cluster+RuN<sub>4</sub> system.

accessibility active sites on the catalysts. The ECSA-normalized LSV curves show that the NMC-Ru<sub>SA+NC</sub> possesses the high specific activity in acidic solution (Fig. S25). The Nyquist plots recorded by EIS measurement (Fig. S26) show that the NMC-Ru<sub>SA+NC</sub> affords the smallest charge transfer resistance among all the investigated catalysts, implying its fast electron transfer ability. Besides, it can be seen in Figs. S27 and S28 that the NMC-Ru<sub>SA+NC</sub> offers a remarkably efficient MA (1.88 A mg<sub>Ru</sub><sup>-1</sup> at  $\eta = 50$  mV) and TOF (3.61 s<sup>-1</sup> at  $\eta = 100$  mV) for comparison with those of the Ru/C (0.71 A mg<sub>Ru</sub><sup>-1</sup> and 1.06 s<sup>-1</sup>) and Pt/C (0.38 A mg<sub>Pt</sub><sup>-1</sup> and 1.01 s<sup>-1</sup>), respectively. As presented in Fig. 4h and Table S7, the NMC-Ru<sub>SA+NC</sub> pays a comparable HER overpotential to other reported Ru-based catalysts, further manifesting its exceptional HER activities in acidic environment. As shown in Fig. S29, the NMC-Ru<sub>SA+NC</sub> exhibits negligible changes of potential after operating over 100 h in acidic solution, indicating its excellent long-term durability. TEM image in Fig. S30a shows that the NMC-Ru<sub>SA+NC</sub> after stability test retains original morphological structure well. The Ru 3p high-resolution XPS spectrum of the NMC-Ru<sub>SA+NC</sub> can be divided into metallic Ru species and Ru<sup>n+</sup> species, accounting for 70.4% and 29.6% of the total Ru content, respectively (Fig. S30b and Table S2). It can be found that the relative content of Ru<sup>n+</sup> species increased and the relative content of

metallic Ru species decreased after stability test, indicating that the Ru nanoclusters were slightly leached due to the corrosiveness of acidic electrolyte. On all these counts, the NMC-Ru<sub>SA+NC</sub> exhibits remarkable electrocatalytic activity as well as long-term stability for HER, enabling their good prospects for practical application in acidic HER.

### 3.4. DFT calculations

To further elucidate the origin of excellent HER activity for the NMC-Ru<sub>SA+NC</sub>, density functional theory (DFT) calculations were carried out to understand the role of coupling active sites between the ultrathin Ru cluster and single Ru atom. Three optimized structural models were deliberately built here based on the experimental results: pure RuN<sub>4</sub> structure (Fig. 5a), pure Ru nanoclusters (Fig. 5b), coupling RuN<sub>4</sub> sites and Ru nanoclusters (Fig. 5c). The charge density distribution of the coupling RuN<sub>4</sub> sites and Ru nanoclusters (Fig. S31) shows that the electron transfers from Ru nanocluster to RuN<sub>4</sub> sites, decoding the strong electronic coupling between the Ru nanoclusters and the RuN<sub>4</sub> sites, which is consistent with the XPS results. The calculated projected density of states (PDOS) of the coupling RuN<sub>4</sub> sites and Ru nanoclusters in Fig. 5d shows that it possesses the metallic character with zero

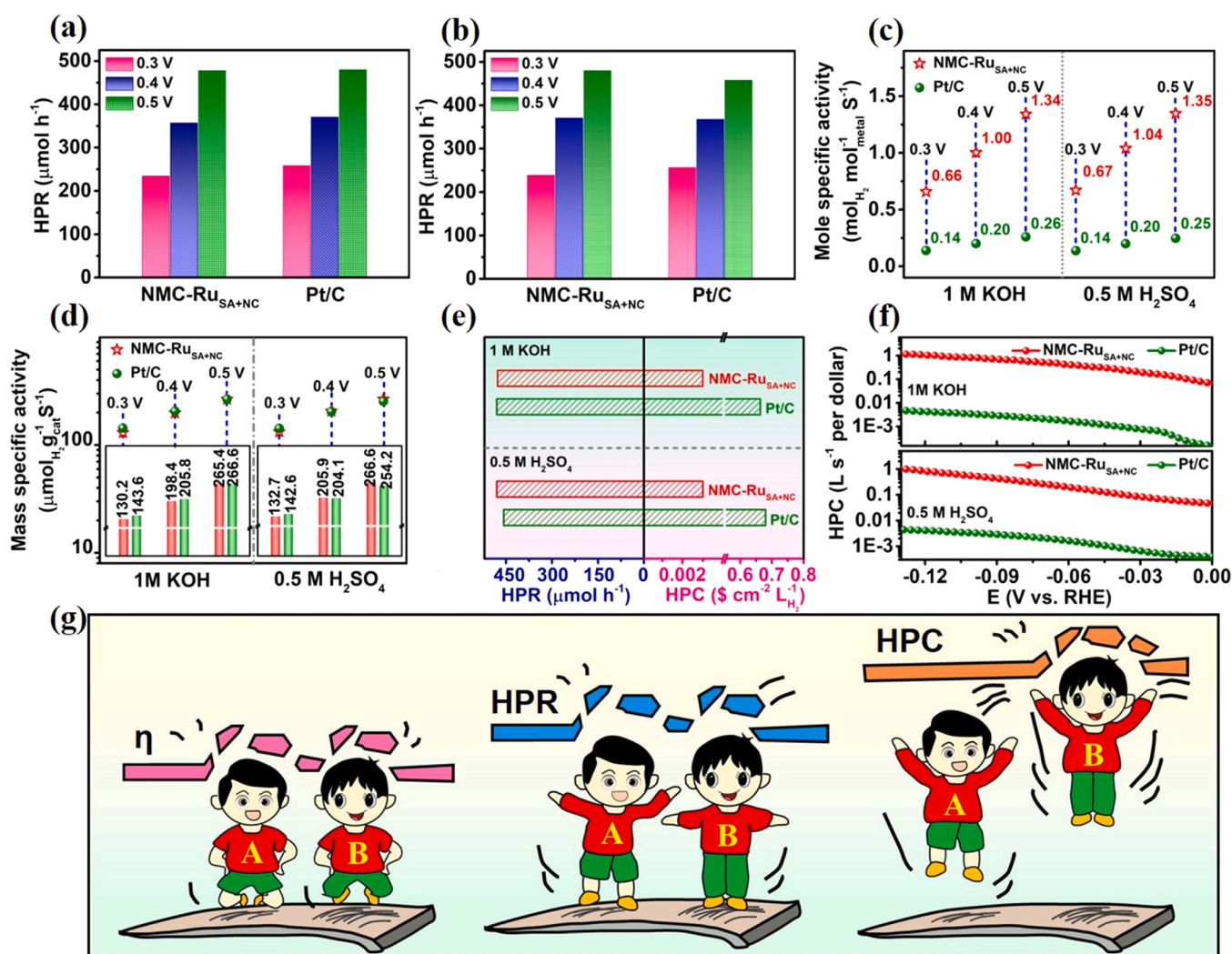


**Fig. 6.** H<sub>2</sub> production rate at the overpotential of 300, 400 and 500 mV without iR correction in (a) 1 M KOH and (b) 0.5 M H<sub>2</sub>SO<sub>4</sub>. A summary of the (c) mole specific activities and (d) mass specific activities of NMC-Ru<sub>SA+NC</sub> and Pt/C. (e) H<sub>2</sub> production rate (left) and corresponding costs (right) at the overpotential of 500 mV without iR correction. (f) Hydrogen production costs obtained from the polarization curves. (g) Schematic diagrams of performance interpretation for Pt/C (named as A) and the NMC-Ru<sub>SA+NC</sub> (named as B), in which HPR represents the H<sub>2</sub> production rate ( $\mu\text{mol h}^{-1}$ ) and HPC means the cost of hydrogen production ( $\text{L s}^{-1}$  per dollar).

bandgap, indicating that the coupling RuN<sub>4</sub> sites and Ru nanoclusters could achieve the fast electron transfer and good electrical conductivity. Besides, it is well known that the position of d band center ( $E_d$ ) relative to the Fermi level ( $E_F$ ) is usually recognized as the indicator of the strength of the metal-adsorbate interaction [1,52,53]. The closer the d band center to Fermi level, the stronger interaction with adsorbed H\* on the metal active sites (M-H); the farther the d band center away from the Fermi level, the weaker the M-H interaction. [1,52] Based on this analysis, the d band center was determined to be  $-0.70$  eV (pure RuN<sub>4</sub> structure),  $-1.44$  eV (coupling RuN<sub>4</sub> sites and Ru nanoclusters) and  $-1.54$  eV (pure Ru nanoclusters), respectively. It can be seen that the introduction of RuN<sub>4</sub> sites in the coupling sites could result in a higher  $E_d$  energy level than pure Ru nanoclusters, indicating that the M-H interaction is reinforced. The pure RuN<sub>4</sub> structure is observed to afford the exorbitant  $E_d$  energy level ( $-0.70$  eV), leading to the excessively strong M-H interaction, which in turn decelerates the desorption of H<sub>2</sub> and thus results in the deactivation of the active sites. Therefore, a proper  $E_d$  energy level, which could balance the adsorption and desorption of the intermediates, could be advantageous to achieving the high intrinsic HER activities for the catalysts (Fig. 5e) [52]. We further calculated the Gibbs free energy of H\* adsorption to investigate the intrinsic HER activities. A moderate  $\Delta G_{H^*}$  close to 0 eV is desired for a superior HER electrocatalyst. As displayed in Fig. 5f, the coupling RuN<sub>4</sub> sites and Ru nanoclusters owns the lowest adsorption energy of H\* ( $-0.026$  eV) among all the investigated models, decoding that the produced strong electronic coupling effect could facilitate the desorption of H\* to generate hydrogen gas. Moreover, the initial Volmer step (water dissociation) was also considered (Fig. 5g). It can be seen that the coupling RuN<sub>4</sub> sites and Ru nanoclusters possesses a lower energy barrier of 0.03 eV than pure Ru nanoclusters (0.77 eV) and RuN<sub>4</sub> sites (0.74 eV), signifying that the coupling RuN<sub>4</sub> sites and Ru nanoclusters could achieve the fast water dissociation, thus enhancing the catalytic HER activity.

In view of the excellent catalytic HER performance of NMC-Ru<sub>SA+NC</sub>, three different Ru sites were also considered for the coupling RuN<sub>4</sub> sites and Ru nanoclusters (Fig. 5h). The electronic structure was analyzed by studying the PDOS of various Ru sites, so as to select potential active sites. As shown in Fig. 5i, it can be seen that the  $E_d$  energy level of Ru1, Ru2, Ru3 sites gradually increase, indicating the intensity of M-H binding from weak to strong. As displayed in Fig. 5j, the Ru2 site exhibit the optimal adsorption strength towards H species with  $\Delta G_{H^*}$  of  $-0.026$  eV, which is much better than that of the Ru1 (0.089 eV) and Ru3 site ( $-0.294$  eV), indicating the dominant role of Ru2 sites in the HER process. This could be attributed to the strong electronic coupling effect between the Ru single atoms and Ru nanoclusters, which enable the Ru2 sites at the interface to dominate the electroactive region (Fig. S31), thus achieving the proper M-H strength and the superior HER performance.

### 3.5. Performance and price evaluation of the catalyst

Some important parameters, i.e. the price of the catalysts, H<sub>2</sub> production rate (HPR), mole specific activity, mass specific activity and H<sub>2</sub> production costs (HPC), were considered to further highlight the significant advantage of the NMC-Ru<sub>SA+NC</sub> for practical application. As is well known, it is crucial to develop the cheap catalysts with comparable catalytic activities and good stability for the realization of the large-scale applications. Noted that the NMC-Ru<sub>SA+NC</sub> affords a low price of 175 \$ m<sup>-2</sup>, which is 11.7 times smaller than that of the Pt/C, suggesting its promising potential for practical applications (Fig. S32, Table S8). As presented in Fig. 6a, b and Tables S9, S10, the HPR of the NMC-Ru<sub>SA+NC</sub> gradually increases with the increase of potential and reaches 477.7 and 479.9  $\mu\text{mol h}^{-1}$  at the overpotential of 500 mV in alkaline and acid environment, respectively, which are comparable to those of the Pt/C (479.9 and 457.6  $\mu\text{mol h}^{-1}$ ). Fig. 6c, d and Tables S11, 12 display that the NMC-Ru<sub>SA+NC</sub> shows remarkable advantages in mole specific

activity and mass specific activity for comparison with the Pt/C, indicating its competitive merits for hydrogen generation in practical applications. Taking the HPR, precious-metal loading and the price into account (the calculation method I [33], see supporting information), the cost for generating per liter H<sub>2</sub> (per unit area) are determined to be 0.0028 \$ cm<sup>-2</sup> L<sub>H<sub>2</sub></sub><sup>-1</sup> for the NMC-Ru<sub>SA+NC</sub> at  $\eta$  of 500 mV in both alkaline and acidic conditions (Fig. 6e and Table S13), which are 231 and 243 times lower than those of commercial Pt/C (0.648 \$ cm<sup>-2</sup> L<sub>H<sub>2</sub></sub><sup>-1</sup> in alkaline and 0.680 \$ cm<sup>-2</sup> L<sub>H<sub>2</sub></sub><sup>-1</sup> in acidic conditions), respectively. Besides, considering the catalytic activities, precious-metal loading and price (the calculation method II, [54,55] see supporting information), the H<sub>2</sub> production per \$ (per unit area) for NMC-Ru<sub>SA+NC</sub> is two orders of magnitude higher than that of the Pt/C in alkaline/acid electrolyte (Fig. 6f). Taken together, it is therefore reasonable to believe that the designed NMC-Ru<sub>SA+NC</sub> not only exhibits the high performance but also greatly reduces the H<sub>2</sub> production costs, endowing it with the huge potential to realize the large-scale commercial use (Fig. 6g).

Beyond that, the catalytic activities and HPR were investigated on the different electrodes with different working areas (Fig. S33) or catalysts loading (Fig. S34). The catalysts modified-carbon cloth with different areas of 0.5, 1, 2, 4 and 9 cm<sup>2</sup> were employed as the working electrodes, on which the equal mass loading (1 mg cm<sup>-2</sup>) is uniformly distributed. As seen from Fig. S33a,c, the LSV curves visibly show that the catalytic activities gradually increased accompanied with the increase of the area of working electrode. It can be found that the 9 cm<sup>2</sup> working electrode merely requires 28 and 45 mV for achieving a current of 100 mA in alkaline and acidic solutions, respectively, which are 70 and 72 mV less than those for the 0.5 cm<sup>2</sup> working electrode. As shown in Fig. S33b,d and Table S14, 15, the HPR shows an increasing upturn as the working area increases at the same applied potential. Moreover, the influence of catalysts loading on HER performance was also explored, showing that the working electrode with 1 mg cm<sup>-2</sup> catalysts loading possesses the best HER activities (Fig. S34). All these results evidence that the NMC-Ru<sub>SA+NC</sub> owns the remarkable advantages for large-scale H<sub>2</sub> production toward industrial applications.

## 4. Conclusions

In summary, Ru single atoms coupling with nanoclusters on the hierarchical porous N-doped carbon have been adopted as the economical and effective catalysts for HER. Experimental and DFT results unveil that the coupling Ru single atoms and nanoclusters could cooperate with each other and produce the strong electronic coupling effects, which could be beneficial to achieving the fast water dissociation and optimized metal-adsorbate H\* strength. Furthermore, the hierarchical porous of NMC-Ru<sub>SA+NC</sub> could effectively facilitate the rapid transport of the reactants to, and removal of the produced H<sub>2</sub> from, these active sites, thus boosting the HER performance at large current densities. Benefiting from the strong electronic coupling effects and fast mass transfer capacity, the obtained NMC-Ru<sub>SA+NC</sub> requires a ultralow overpotential for achieving a high current density of 500 mA cm<sup>-2</sup> in 1.0 M KOH (185 mV) and 0.5 M H<sub>2</sub>SO<sub>4</sub> (161 mV). Moreover, it affords the higher MA and TOF than those of Pt/C and other recently reported Ru-based HER electrocatalysts. More importantly, the cost for generating per liter H<sub>2</sub> is determined to be 0.0028 \$ cm<sup>-2</sup> L<sub>H<sub>2</sub></sub><sup>-1</sup> for the NMC-Ru<sub>SA+NC</sub> in both alkaline and acidic conditions, 231 and 243 times lower than those of commercial Pt/C (0.648 \$ cm<sup>-2</sup> L<sub>H<sub>2</sub></sub><sup>-1</sup> in alkaline and 0.680 \$ cm<sup>-2</sup> L<sub>H<sub>2</sub></sub><sup>-1</sup> in acidic condition), respectively, testifying the remarkable advantages and good prospects for practical application. This work offers an in-depth understanding of the strong electronic coupling effect and fast mass transfer capacity to construct an economical and effective HER catalysts for guaranteeing the high-throughput H<sub>2</sub> production in practical applications.

## CRediT authorship contribution statement

**Hanxu Yao:** Conceptualization, Methodology, Validation, Investigation, Data curation, Writing – original draft. **Xingkun Wang:** Conceptualization, Methodology, Validation, Investigation, Data curation, Writing – original draft. **Kai Li:** Methodology, Investigation, Data curation. **Cheng Li:** Methodology, Validation, Data curation. **Canhui Zhang:** Investigation, Data curation. **Jian Zhou:** Validation, Investigation, Data curation. **Zhengwen Cao:** Methodology, Data curation. **Huanlei Wang:** Methodology, Validation, Data curation. **Meng Gu:** Methodology, Validation, Investigation, Data curation. **Minghua Huang:** Conceptualization, Methodology, Validation, Writing – review & editing, Resources, Supervision. **Heqing Jiang:** Conceptualization, Methodology, Validation, Investigation, Data curation, Writing – original draft, Supervision.

## Declaration of Competing Interest

The authors declare that they have no known competing financial interests or personal relationships that could have appeared to influence the work reported in this paper.

## Acknowledgements

This work was financially supported by the National Natural Science Foundation of China (21775142), China; the Key Research & Development Project of Shandong (Major Innovation Projects) (Grant No. 2019JZZY010905), China; and the Natural Science Foundation of Shandong Province (ZR2020ZD10), China.

## Appendix A. Supporting information

Supplementary data associated with this article can be found in the online version at doi:10.1016/j.apcatb.2022.121378.

## References

- [1] Y.J. Li, Y.J. Sun, Y.N. Qin, W.Y. Zhang, L. Wang, M.C. Luo, H. Yang, S.J. Guo, Recent advances on water-splitting electrocatalysis mediated by noble-metal-based nanostructured materials, *Adv. Energy Mater.* 10 (2020) 1903120.
- [2] H. Jiang, M.Z. Sun, S.L. Wu, B.L. Huang, C.S. Lee, W.J. Zhang, Oxygen-incorporated NiMoP nanotube arrays as efficient bifunctional electrocatalysts for urea-assisted energy-saving hydrogen production in alkaline electrolyte, *Adv. Funct. Mater.* 31 (2021) 2104951.
- [3] Q.F. Yang, C.J. Zhang, B. Dong, Y.C. Cui, F. Wang, J.H. Cai, P. Jin, L. Feng, Synergistic modulation of nanostructure and active sites: Ternary Ru&Fe-WO<sub>x</sub> electrocatalyst for boosting concurrent generations of hydrogen and formate over 500 mA cm<sup>-2</sup>, *Appl. Catal. B Environ.* 296 (2021), 120359.
- [4] J.C. Li, C. Zhang, T. Zhang, Z.H. Shen, Q.W. Zhou, J. Pu, H.J. Ma, T.H. Wang, H. G. Zhang, H.M. Fan, Y.Y. Wang, H.X. Ma, Multiple-interface relay catalysis: Enhancing alkaline hydrogen evolution through a combination of Volmer promoter and electrical-behavior regulation, *Chem. Eng. J.* 397 (2020), 125457.
- [5] J. Yin, J. Jin, H. Zhang, M. Lu, Y. Peng, B.L. Huang, P.X. Xi, C.H. Yan, Atomic arrangement in metal-doped NiS<sub>2</sub> boosts the hydrogen evolution reaction in alkaline media, *Angew. Chem. Int. Ed.* 58 (2019) 18676–18682.
- [6] W.D. Li, Y.X. Zhao, Y. Liu, M.Z. Sun, G.I.N. Waterhouse, B.L. Huang, K. Zhang, T. R. Zhang, S.Y. Lu, Exploiting Ru-induced lattice strain in CoRu nanoalloys for robust bifunctional hydrogen production, *Angew. Chem. Int. Ed.* 60 (2021) 3290–3298.
- [7] N. Wang, S.L. Ning, X.L. Yu, D. Chen, Z.L. Li, J.C. Xu, H. Meng, D.K. Zhao, L.G. Li, Q.M. Liu, B.Z. Lu, S.W. Chen, Graphene composites with Ru-RuO<sub>2</sub> heterostructures: Highly efficient Mott-Schottky-type electrocatalysts for pH-universal water splitting and flexible zinc-air batteries, *Appl. Catal. B Environ.* 302 (2022), 120838.
- [8] F. Zhou, Y. Zhou, G.G. Liu, C.T. Wang, J. Wang, Recent advances in nanostructured electrocatalysts for hydrogen evolution reaction, *Rare Met.* 40 (2021) 3375–3405.
- [9] G.H. Gu, J. Lim, C.Z. Wan, T. Cheng, H.T. Pu, S. Kim, J. Noh, C. Choi, J. Kim, W. A. Goddard, X.F. Duan, Y. Jung, Autobifunctional mechanism of jagged Pt nanowires for hydrogen evolution kinetics via end-to-end simulation, *J. Am. Chem. Soc.* 143 (2021) 7590.
- [10] T. Wu, J. Hong, Z.W. Lu, H.Y. Wu, C.Z. Wu, Z.B. Tang, X.H. Liu, B.R. Zeng, Y.T. Xu, G.R. Chen, C.H. Yuan, L.Z. Dai, In-situ generation of Ru-catechol coordinative polymer precursor for high-performance hydrogen evolution reaction doped carbon catalyst, *Appl. Catal. B Environ.* 285 (2021), 119795.
- [11] B. Tang, X.D. Yang, Z.H. Kang, L.G. Feng, Crystallized RuTe<sub>2</sub> as unexpected bifunctional catalyst for overall water splitting, *Appl. Catal. B Environ.* 278 (2020), 119281.
- [12] R.P. Ma, Y. Wang, G.Q. Li, L. Yang, S.W. Liu, Z. Jin, X. Zhao, J.J. Ge, W. Xing, Tuning the oxidation state of Ru to surpass Pt in hydrogen evolution reaction, *Nano Res.* 14 (2021) 4321–4327.
- [13] D.H. Kweon, M.S. Okyay, S.J. Kim, J.P. Jeon, H.J. Noh, N. Park, J. Mahmood, J. B. Baek, Ruthenium anchored on carbon nanotube electrocatalyst for hydrogen production with enhanced Faradaic efficiency, *Nat. Commun.* 11 (2020) 1278.
- [14] C. Zhang, Y.T. Luo, J.Y. Tan, Q.M. Yu, F.N. Yang, Z.Y. Zhang, L.S. Yang, H. M. Cheng, B.L. Liu, High-throughput production of cheap mineral-based two-dimensional electrocatalysts for high-current-density hydrogen evolution, *Nat. Commun.* 11 (2020) 3724.
- [15] J.C. Li, C. Zhang, C. Zhang, H.J. Ma, Y. Yang, Z.Q. Guo, Y.Y. Wang, H.X. Ma, Electronic configuration of single ruthenium atom immobilized in urchin-like tungsten trioxide towards hydrazine oxidation-assisted hydrogen evolution under wide pH media, *Chem. Eng. J.* 430 (2022), 132953.
- [16] J.W. Su, Y. Yang, G.L. Xia, J.T. Chen, P. Jiang, Q.W. Chen, Ruthenium-cobalt nanoalloys encapsulated in nitrogen-doped graphene as active electrocatalysts for producing hydrogen in alkaline media, *Nat. Commun.* 8 (2017) 14969.
- [17] Y.H. Wang, R.Q. Li, H.B. Li, H.L. Huang, Z.J. Guo, H.Y. Chen, Y. Zheng, K.G. Qu, Controlled synthesis of ultrasmall RuP<sub>2</sub> particles on N,P-codoped carbon as superior pH-wide electrocatalyst for hydrogen evolution, *Rare Met.* 40 (2021) 1040–1047.
- [18] X.K. Wu, Z.C. Wang, D. Zhang, Y.N. Qin, M.H. Wang, Y. Han, T.R. Zhan, B. Yang, S. X. Li, J.P. Lai, L. Wang, Solvent-free microwave synthesis of ultra-small Ru-Mo<sub>2</sub>C@CNT with strong metal-support interaction for industrial hydrogen evolution, *Nat. Commun.* 12 (2021) 4018.
- [19] J.M. Ge, D.B. Zhang, Y. Qin, T. Dou, M.H. Jiang, F.Z. Zhang, X.D. Lei, Dual-metallic single Ru and Ni atoms decoration of MoS<sub>2</sub> for high-efficiency hydrogen production, *Appl. Catal. B Environ.* 298 (2021), 120557.
- [20] J. Wang, W.H. Fang, Y. Hu, Y.H. Zhang, J.Q. Dang, Y. Wu, B.Z. Chen, H. Zhao, Z. X. Li, Single atom Ru doping 2H-MoS<sub>2</sub> as highly efficient hydrogen evolution reaction electrocatalyst in a wide pH range, *Appl. Catal. B Environ.* 298 (2021), 120490.
- [21] J.C. Li, Y. Li, J.A. Wang, C. Zhang, H.J. Ma, C.H. Zhu, D.D. Fan, Z.Q. Guo, M. Xu, Y. Y. Wang, H.X. Ma, Elucidating the critical role of ruthenium single atom sites in water dissociation and dehydrogenation behaviors for robust hydrazine oxidation-boosted alkaline hydrogen evolution, *Adv. Funct. Mater.* (2022) 2109439.
- [22] J.C. Li, C. Zhang, H.J. Ma, T.H. Wang, Z.Q. Guo, Y. Yang, Y.Y. Wang, H.X. Ma, Modulating interfacial charge distribution of single atoms confined in molybdenum phosphosulfide heterostructures for high efficiency hydrogen evolution, *Chem. Eng. J.* 414 (2021), 128834.
- [23] C. Hu, E.H. Song, M.Y. Wang, W. Chen, F.Q. Huang, Z.X. Feng, J.J. Liu, J.C. Wang, Partial-single-atom, partial-nanoparticle composites enhance water dissociation for hydrogen evolution, *Adv. Sci.* 8 (2021) 2001881.
- [24] J. Yang, H. Guo, S.L. Chen, Y.L. Li, C. Cai, P. Gao, L.P. Wang, Y.N. Zhang, R.J. Sun, X.B. Niu, Z.M. Wang, Anchoring and space-confinement effects to form ultrafine Ru nanoclusters for efficient hydrogen generation, *J. Mater. Chem. A* 6 (2018) 13859–13866.
- [25] L.J. Zhang, H. Jang, Y. Wang, Z.J. Li, W. Zhang, M.G. Kim, D.J. Yang, S.G. Liu, X. E. Liu, J. Cho, Exploring the dominant role of atomic- and nano-ruthenium as active sites for hydrogen evolution reaction in both acidic and alkaline media, *Adv. Sci.* 8 (2021) 2004516.
- [26] K.J. Tu, D. Tranca, F. Rodriguez-Hernandez, K.Y. Jiang, S.H. Huang, Q. Zheng, M. X. Chen, C.B. Lu, Y.Z. Su, Z.Y. Chen, H.Y. Mao, C.Q. Yang, J.Y. Jiang, H.W. Liang, X.D. Zhuang, A novel heterostructure based on RuMo nanoalloys and N-doped carbon as an efficient electrocatalyst for the hydrogen evolution reaction, *Adv. Mater.* 32 (2020) 2005433.
- [27] W. Li, H. Zhang, K. Zhang, W. Hu, Z. Cheng, H. Chen, X. Feng, T. Peng, Z. Kou, Monodispersed ruthenium nanoparticles interfacially bonded with defective nitrogen-and-phosphorus-doped carbon nanosheets enable pH-universal hydrogen evolution reaction, *Appl. Catal. B Environ.* 306 (2022), 121095.
- [28] J. Cai, R. Javed, D.X. Ye, H.B. Zhao, J.J. Zhang, Recent progress in noble metal nanocluster and single atom electrocatalysts for the hydrogen evolution reaction, *J. Mater. Chem. A* 8 (2020) 22467–22487.
- [29] Y.J. Yang, Y.H. Yu, J. Li, Q.R. Chen, Y.L. Du, P. Rao, R.S. Li, C.M. Jia, Z.Y. Kang, P. L. Deng, Y.J. Shen, X.L. Tian, Engineering ruthenium-based electrocatalysts for effective hydrogen evolution reaction, *Nano Micro Lett.* 13 (2021) 160.
- [30] F.F. Zhang, Y.L. Zhu, Q. Lin, L. Zhang, X.W. Zhang, H.T. Wang, Noble-metal single-atoms in thermocatalysis, electrocatalysis, and photocatalysis, *Energy Environ. Sci.* 14 (2021) 2954–3009.
- [31] Q. Hu, G.M. Li, X.W. Huang, Z.Y. Wang, H.P. Yang, Q.L. Zhang, J.H. Liu, C.X. He, Electronic structure engineering of single atomic Ru by Ru nanoparticles to enable enhanced activity for alkaline water reduction, *J. Mater. Chem. A* 7 (2019) 19531–19538.
- [32] Q. Zhang, W. Xiao, W.H. Guo, Y.X. Yang, J.L. Lei, H.Q. Luo, N.B. Li, Macroporous array induced multiscale modulation at the surface/interface of Co(OH)<sub>2</sub>/NiMo self-supporting electrode for effective overall water splitting, *Adv. Funct. Mater.* 31 (2021) 2102117.
- [33] F.N. Yang, Y.T. Luo, Q.M. Yu, Z.Y. Zhang, S. Zhang, Z.B. Liu, W.C. Ren, H. M. Cheng, J. Li, B.L. Liu, A durable and efficient electrocatalyst for saline water splitting with current density exceeding 2000 mA cm<sup>-2</sup>, *Adv. Funct. Mater.* 31 (2021) 2010367.

- [34] J. Wang, F. Xu, H.Y. Jin, Y.Q. Chen, Y. Wang, Non-noble metal-based carbon composites in hydrogen evolution reaction: fundamentals to applications, *Adv. Mater.* 29 (2017) 1605838.
- [35] Y.T. Luo, L. Tang, U. Khan, Q.M. Yu, H.M. Cheng, X.L. Zou, B.L. Liu, Morphology and surface chemistry engineering toward pH-universal catalysts for hydrogen evolution at high current density, *Nat. Commun.* 10 (2019) 269.
- [36] B.Z. Lu, L. Guo, F. Wu, Y. Peng, J.E. Lu, T.J. Smart, N. Wang, Y.Z. Finfrock, D. Morris, P. Zhang, N. Li, P. Gao, Y. Ping, S.W. Chen, Ruthenium atomically dispersed in carbon outperforms platinum toward hydrogen evolution in alkaline media, *Nat. Commun.* 10 (2019) 631.
- [37] J.N. Tiwari, A.M. Harzandi, M. Ha, S. Sultan, C.W. Myung, H.J. Park, D.Y. Kim, P. Thangavel, A.N. Singh, P. Sharma, S.S. Chandrasekaran, F. Salehnia, J.W. Jang, H.S. Shin, Z. Lee, K.S. Kim, High-performance hydrogen evolution by Ru single atoms and nitrided-Ru nanoparticles implanted on N-doped graphitic sheet, *Adv. Energy Mater.* 9 (2019) 1900931.
- [38] J. Xiong, J. Li, J.W. Shi, X.L. Zhang, N.T. Suen, Z. Liu, Y.J. Huang, G.X. Xu, W. W. Cai, X.R. Lei, L.G. Feng, Z.H. Yang, L. Huang, H.S. Cheng, In situ engineering of double-phase interface in Mo/Mo<sub>2</sub>C heteronanoseeds for boosted hydrogen evolution reaction, *ACS Energy Lett.* 3 (2018) 341–348.
- [39] Y.L. Wu, X.F. Li, Y.S. Wei, Z.M. Fu, W.B. Wei, X.T. Wu, Q.L. Zhu, Q. Xu, Ordered macroporous superstructure of nitrogen-doped nanoporous carbon implanted with ultrafine Ru nanoclusters for efficient pH-universal hydrogen evolution reaction, *Adv. Mater.* 33 (2021) 2006965.
- [40] H. Li, M.T. Zhang, L.C. Yi, Y.J. Liu, K. Chen, P. Shao, Z.H. Wen, Ultrafine Ru nanoparticles confined in 3D nitrogen-doped porous carbon nanosheet networks for alkali-acid Zn-H<sub>2</sub> hybrid battery, *Appl. Catal. B Environ.* 280 (2021), 119412.
- [41] C.B. Hong, X.F. Li, W.B. Wei, X.T. Wu, Q.L. Zhu, Nano-engineering of Ru-based hierarchical porous nanoreactors for highly efficient pH-universal overall water splitting, *Appl. Catal. B Environ.* 294 (2021), 120230.
- [42] D. Cao, J.Y. Wang, H.X. Xu, D.J. Cheng, Construction of dual-site atomically dispersed electrocatalysts with Ru-C<sub>5</sub> single atoms and Ru-O<sub>4</sub> nanoclusters for accelerated alkali hydrogen evolution, *Small* 17 (2021) 2101163.
- [43] Q.J. Xie, Z. Wang, L.K. Lin, Y. Shu, J.J. Zhang, C. Li, Y.H. Shen, H. Uyama, Nanoscaled and atomic ruthenium electrocatalysts confined inside super-hydrophilic carbon nanofibers for efficient hydrogen evolution reaction, *Small* 17 (2021) 2102160.
- [44] Y.Z. Li, J. Abbott, Y.C. Sun, J.M. Sun, Y.C. Du, X.J. Han, G. Wu, P. Xu, Ru nanoassembly catalysts for hydrogen evolution and oxidation reactions in electrolytes at various pH values, *Appl. Catal. B Environ.* 258 (2019), 117952.
- [45] Y. Liu, N. Chen, W. Li, M. Sun, T. Wu, B. Huang, X. Yong, Q. Zhang, L. Gu, H. Song, R. Bauer, J.S. Tse, S.Q. Zang, B. Yang, S. Lu, Engineering the synergistic effect of carbon dots-stabilized atomic and subnanometric ruthenium as highly efficient electrocatalysts for robust hydrogen evolution, *SmartMat* (2021) 1–11, <https://doi.org/10.1002/smm2.1067.X>.
- [46] X.K. Wang, G. Zhan, Y. Wang, Y. Zhang, J. Zhou, R. Xu, H. Gai, H. Wang, H. Q. Jiang, M.H. Huang, Engineering core-shell Co<sub>9</sub>S<sub>8</sub>/Co nanoparticles on reduced graphene oxide: Efficient bifunctional Mott-Schottky electrocatalysts in neutral rechargeable Zn-Air batteries, *J. Energy Chem.* 68 (2022) 113–123.
- [47] Z.W. Che, X.Y. Lu, B.F. Cai, X.X. Xu, J.C. Bao, Y. Liu, Ligand-controlled synthesis of high density and ultra-small Ru nanoparticles with excellent electrocatalytic hydrogen evolution performance, *Nano Res.* 15 (2022) 1269–1275.
- [48] Y.J. Yin, Y. Tan, Q.Y. Wei, S.C. Zhang, S.Q. Wu, Q. Huang, F.L. Hu, Y. Mi, Nanovilli electrode boosts hydrogen evolution: A surface with superaerophobicity and superhydrophilicity, *Nano Res.* 14 (2021) 961–968.
- [49] J. Yu, Q.J. He, G.M. Yang, W. Zhou, Z.P. Shao, M. Ni, Recent advances and prospective in ruthenium-based materials for electrochemical water splitting, *ACS Catal.* 9 (2019) 9973–10011.
- [50] P.P. Su, W. Pei, X.W. Wang, Y.F. Ma, Q.K. Jiang, J. Liang, S. Zhou, J.J. Zhao, J. Liu, G.Q. Lu, Exceptional electrochemical HER performance with enhanced electron transfer between Ru nanoparticles and single atoms dispersed on a carbon substrate, *Angew. Chem. Int. Ed.* 60 (2021) 16044–16050.
- [51] J. Yu, Y.N. Guo, S.X. She, S.S. Miao, M. Ni, W. Zhou, M.L. Liu, Z.P. Shao, Bigger is surprisingly better: agglomerates of larger RuP nanoparticles outperform benchmark Pt nanocatalysts for the hydrogen evolution reaction, *Adv. Mater.* 30 (2018) 1800047.
- [52] C. Wei, Y.M. Sun, G.G. Scherer, A.C. Fisher, M. Sherburne, J.W. Ager, Z.C.J. Xu, Surface composition dependent ligand effect in tuning the activity of nickel-copper bimetallic electrocatalysts toward hydrogen evolution in alkaline, *J. Am. Chem. Soc.* 142 (2020) 7765–7775.
- [53] H.B. Zhang, W. Zhou, X.F. Lu, T. Chen, X.W. Lou, Implanting isolated Ru atoms into edge-rich carbon matrix for efficient electrocatalytic hydrogen evolution, *Adv. Energy Mater.* 10 (2020) 2000882.
- [54] K. Li, Y. Li, Y.M. Wang, J.J. Ge, C.P. Liu, W. Xing, Enhanced electrocatalytic performance for the hydrogen evolution reaction through surface enrichment of platinum nanoclusters alloying with ruthenium in situ embedded in carbon, *Energy Environ. Sci.* 11 (2018) 1232–1239.
- [55] T.T. Liu, W.B. Gao, Q.Q. Wang, M.L. Dou, Z.P. Zhang, F. Wang, Selective loading of atomic platinum on a RuCeO<sub>x</sub> support enables stable hydrogen evolution at high current densities, *Angew. Chem. Int. Ed.* 59 (2020) 20423–20427.